

Modelling of Blast Furnace with Respective Chemical Reactions in Coke and Ore Burden Layers



XIAOBING YU and YANSONG SHEN

The ironmaking blast furnace (BF) is an efficient chemical reactor for producing liquid iron from solid iron ore, where the solids of coke and iron ore are charged in alternative layers and different chemical reactions occur in the two solid layers as they descend. Such respective reacting burden layers have not been considered explicitly in the previous BF models. In this article, a mathematical model based on multi-fluid theory is developed for describing the multiphase reacting flows considering the respective reacting burden layers. Then, this model is applied to a BF, covering the area from the burden surface at the furnace top to the liquid surface above the hearth, to describe the inner states of a BF in terms of the multiphase flows, temperature distribution and reduction process. The results show that some key important features in the layered burden with respective chemical reactions are captured, including fluctuating iso-lines in terms of gas flow and thermochemical behaviours; particularly the latter cannot be well captured in the previous BF models. The temperature difference between gas–solid phases is found to be larger near the raceway, at the cohesive zone and at the furnace top, and the thermal reserved zone can be identified near the shaft. Three chemical reserve zones of hematite, magnetite and wustite can also be observed near the stockline, in the shaft near the wall and near centre, respectively. Inside each reserve zone, the corresponding ferrous oxides stay constantly high in alternative layers; the overall performance indicators including gas utilization efficiency and reduction degree also stay stable in an alternative-layered structure. This model provides a cost-effective tool to investigate the BF in-furnace process and optimize BF operation.

<https://doi.org/10.1007/s11663-018-1332-6>

© The Minerals, Metals & Materials Society and ASM International 2018

I. INTRODUCTION

AS a typical and efficient chemical reactor in the ironmaking process, a blast furnace (BF) consumes iron ore, flux and coke to produce liquid iron and slag and discharges them through tapholes. The solids of coke and iron ore are charged in alternative layers from the furnace top. A hot blast is injected through tuyeres at the lower part of the BF at a relatively high speed of typically ~ 240 m/s and high temperature of typically 1200 °C, forming a void termed the raceway. Inside the raceway, reducing gas is produced by the intense combustion of coke. It then flows upward through gaps between the descending solid particles or liquid droplets toward the furnace top.^[1] During this process, mass, momentum and heat are exchanged among gas, solid and liquid phases and then different chemical reactions

occur in different regions; particularly different chemical reactions occur in different solid layers. For example, in the shaft of BFs, inside the coke layers, a carbon solution reaction takes place, while inside iron ore layers, ferrous oxides reduction happens. Thus, a layered structure of ore and coke with respective chemical reactions is an important feature in solid distributions in terms of the flow, temperature, component and performance indicators. The schematic of an ironmaking BF and respective chemical reactions in alternative burden layers is shown in Figure 1. The in-furnace phenomena of BF are thus very complex, and it is important to understand the internal state and furnace performance when considering different chemical reactions in alternative layers of iron ore and coke, respectively.

Many efforts have been made to understand and optimize the ironmaking BF process, particularly its internal state, mainly through experimental and mathematical approaches. Some researchers dissected BFs^[2–6] to obtain such in-furnace information. Some quantity indexes of smelting could be directly measured or observed, for example, the cohesive zone's location and shape and the stagnant region's presence near the

XIAOBING YU and YANSONG SHEN are with the School of Chemical Engineering, University of New South Wales, Sydney, NSW 2052, Australia. Contact e-mail: ys.shen@unsw.edu.au

Manuscript submitted April 3, 2018.

Article published online July 16, 2018.

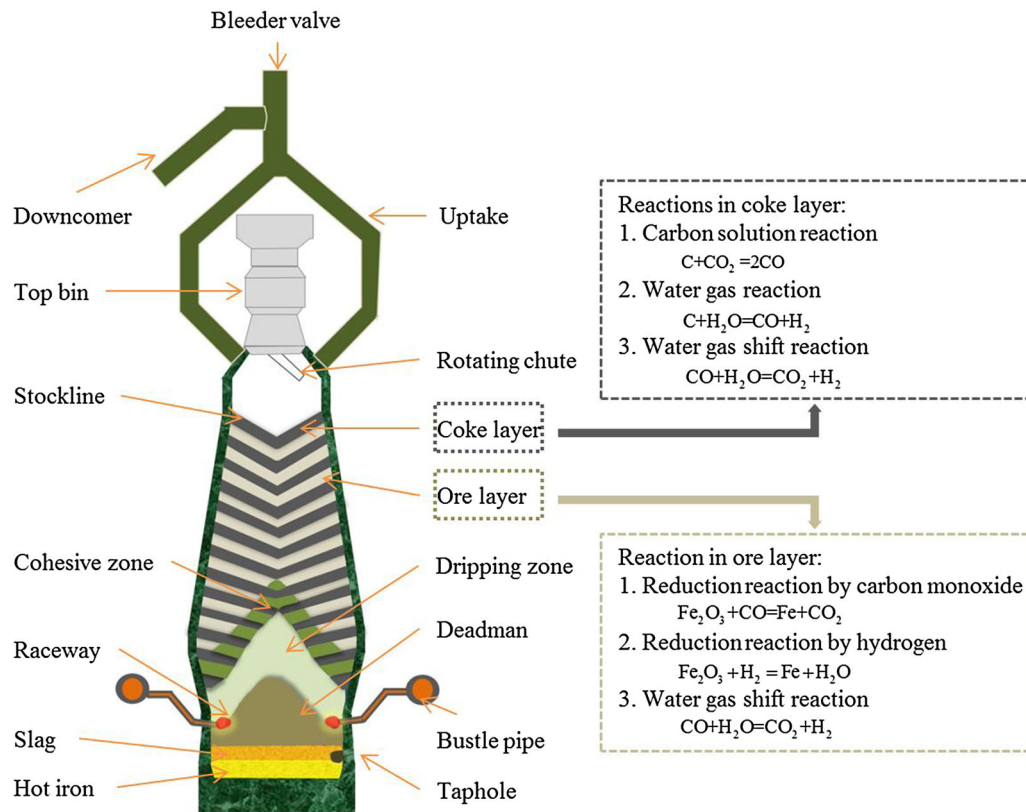


Fig. 1—Schematic of an ironmaking BF with key chemical reactions in alternative coke and ore burden layers.

hearth centre. However, this dissection approach is a large-scale project and thus investment- and labour-consuming. Moreover, it is difficult to capture the in-furnace phenomena in an active BF because of the high-pressure and high-temperature in-furnace conditions. Another important method of BF study is physical experiments, ranging from the laboratory to pilot scale. This method could provide measurable and quantitative information, such as the flow dynamics and reaction kinetics related to BF operation at the laboratory/pilot scale. Nevertheless, the complexity of BFs involving flow, heat transfer and chemical reactions poses a practical and theoretical challenge when scaling up those experiments. Additionally, the experimental investigations are not cost effective.

Recently, many researchers use mathematical models to study BF in-furnace phenomena. A mathematical model can capture the main characteristics inside a BF and, to some extent, predict some phenomena. Moreover, in most cases, the mathematical model is a cost-effective and time-efficient method compared with industry tests and laboratory- and pilot-scale experiments. So far, there are two main approaches to BF multiphase flow modelling, namely, the continuum- and discrete-based methods.^[7-9] Briefly, the former is based on the Navier–Stokes equation, which considers the effect of viscosity on fluid dynamics, and the latter mainly solves Newton’s Second Law for describing particle translational and rotational movements, respectively. In the continuum-based method, a phase is

treated as a continuum. It uninterruptedly occupies the flow domain with no consideration of particle interactions. This method, coupled with various sub-models in terms of phase momentum transport, heat transfer and chemical reactions, has been proved to be successful and effective in the simulation of the in-furnace phenomenon of a BF. The discrete-based method is more accurate in the modelling of solid flow since it solves force equations for every particle simultaneously. However, this method is constrained by its massive computational demand and thus cannot be directly used in industrial-scale simulations. To date, the continuum-based approach remains the dominant method for BF modelling and optimization. A two-dimensional (2D) axisymmetric model is widely used in BF modelling for simplicity and computational efficiency^[10-13] and is considered adequate to capture the main features of phenomena inside a BF such as axisymmetric flow patterns and thermochemical behaviours, which is actually the case in BF practice under normal operations. They are mainly used to investigate BF operations at the furnace top. Some three-dimensional (3D) BF models have been reported. They are mainly for investigating BF operations at tuyeres.^[14] These BF models are based on a continuum approach and usually have used a mixture treatment for solid phase,^[10,15-18] where ore and coke are mixed well. Recently, a layered structure treatment has also been used.^[12,19,21,24,26] Such layered treatment of the solid structure makes the solid distribution calculation and cohesive zone prediction more realistic. Furthermore,

the layered burden structure with respective chemical reactions was considered in a reduction process of iron ore in a packed bed using the Euler–Lagrange approach, the so-called discrete-based method.^[20] It was observed that the reaction rate, temperature field and monoxide-hydrogen gas concentration were quite different in the adjacent coke and ore layers, indicating the significance of the consideration of respective chemical reactions in a layered burden structure in a reduction process. However, a layered burden structure with respective chemical reactions was not well considered in previous BF modelling papers.^[9,21–26] Fu *et al.* reported a comprehensive BF model considering different chemical reactions in different burden layers,^[13] but the alternative-layered distribution of the gas components and three ferrous oxides was not well captured.

In this article, a mathematical model is developed based on the framework of a previous work.^[12,25] In this model, a layered structure of ore and coke layers with respective chemical reactions in respective layers is considered explicitly, *namely*, the reactions related to three ferrous oxides occur in ore layers and the reactions related to coke take place in coke layers only. The typical in-furnace phenomena such as the multiphase flow, temperature field and species distribution will be simulated. More importantly, the features related to respective chemical reactions in respective layers will be captured. Moreover, BF performance indicators will be predicted and compared with the measurements such as the top gas components and utilization efficiency.

II. MODEL DESCRIPTION

The present model is developed based on the framework of a previous work^[12,25] and is outline below for completion. The new developments are also described. The present model is a 2D axisymmetric model, which

considers gas–solid–liquid flow, heat transfer and chemical reactions. The calculation domain of this model ranges from the surface of the liquid phase in the hearth to the stockline level near the furnace throat. Liquid flow inside the furnace hearth is not considered. Gas phase is regarded as a compressible Newtonian fluid with its density solved based on the ideal gas equation. Solid phases, including both coke and ore, are treated as incompressible fluids with constant viscosity. The mixed layers between the coke and ore layers are neglected for simplicity. In this article, the BF model is treated as a steady-state model. This is because, in typical BFs, the velocity of the solid phase is much smaller compared with gas velocity, and as a result, the residence time of the solid phase in BFs is much longer than the gas phase (*i.e.*, the residence time of the solid could be over hours while that of gas is only several seconds^[27]). Moreover, blast operations at the lower part of the BF including the blast rate, temperature and composition are usually stable in normal BF operations.^[28,29] Although coke and ore are charged periodically from the furnace top, the productivity of the BF operation is very stable. In addition, the steady-state model has been widely adopted in many recent papers on BF modelling^[12–14,19,24–26] and has been proved effective in simulating the internal state of a BF.

A. Governing Equations

The governing equations of this model are listed in Table I. In this work, gas flow is modelled by the Navier–Stokes equation. The SIMPLE method^[30] is used to acquire the correct velocity and pressure distribution considering their proven reliability. To be specific, the gas phase is treated as a mixture of CO, CO₂, H₂, H₂O and N₂. The solid phase, including ore and coke, is modelled using the so-called viscous model.^[10] In this, the solid is regarded as one kind of

Table I. Governing Equations of This BF Model

Governing Equations	Description
Mass Conservation	$\nabla \cdot (\varepsilon_i \rho_i \mathbf{u}_i) = S_i$, where $S_i = -\sum_k \beta_{i,k} R_k^*$
Momentum Conservation—Gas	$\nabla \cdot (\varepsilon_g \rho_g \mathbf{u}_g \mathbf{u}_g) = \nabla \cdot \boldsymbol{\tau}_g - \varepsilon_g \nabla P_g + \rho_g \varepsilon_g \mathbf{g} + \mathbf{F}_g^s + \mathbf{F}_g^{l,d}$ $\boldsymbol{\tau}_g = \varepsilon_g \mu_g \left[\nabla \mathbf{u}_g + (\nabla \mathbf{u}_g)^T \right] - \frac{2}{3} \varepsilon_g \mu_g (\nabla \mathbf{u}_g) \mathbf{I}$
Momentum Conservation—Solid	$\nabla \cdot (\varepsilon_s \rho_s \mathbf{u}_s \mathbf{u}_s) = \nabla \cdot \boldsymbol{\tau}_s - \varepsilon_s \nabla P_s + \rho_s \varepsilon_s \mathbf{g}$ $\boldsymbol{\tau}_s = \varepsilon_s \mu_s \left[\nabla \mathbf{u}_s + (\nabla \mathbf{u}_s)^T \right] - \frac{2}{3} \varepsilon_s \mu_s (\nabla \mathbf{u}_s) \mathbf{I}$
Momentum Conservation—Liquid	$\mathbf{F}_{l,d}^g + \mathbf{F}_{l,d}^s + \varepsilon_{l,d} \rho_l \mathbf{g} = 0$
Heat and Species Conservation	$\nabla \cdot (\varepsilon_i \rho_i \mathbf{u}_i \phi_{i,m}) - \nabla \cdot (\varepsilon_i \Gamma_i \nabla \phi_{i,m}) = S_{\phi_{i,m}}$ if $\phi_{i,m}$ is $H_{i,m}$, $\Gamma_i = \lambda_i / c_{p,i}$ $S_{\phi_{i,m}} = \delta_i h_{ij} \alpha (T_i - T_j) + c_{p,i} T_i \delta_i \sum_k \sum_l \beta_{k,l} R_k^* + \eta_i \sum_k R_k^* (-\Delta H_k)$
Phase Volume Fraction	if $\phi_{i,m}$ is $w_{i,m}$, $\Gamma_i = \rho_i D_i$, $S_{\phi_{i,m}} = \sum_k \alpha_{i,m,k} R_k^*$, where
Ideal Gas Equation	$\phi_{i,m} = w_{g,co}, w_{g,co_2}, w_{s,Fe_2O_3}, w_{s,Fe_3O_4}, w_{s,FeO}, w_{s,flux}$ $\sum_i \varepsilon_i = 1$ $p_g^i = \sum_i (y_i M_i) RT_g / V_g$

Table II. Interaction Forces and Heat Transfer Between Phases

Description	Phases	Equations
Momentum Transfer	gas–solid	$\mathbf{F}_g^s = -\mathbf{F}_s^g = -\left(\alpha_f \rho_g \mathbf{u}_g^s + \beta_f\right) \mathbf{u}_g^s$ <p>where $\alpha_f = 1.75(1 - \varepsilon_g)/d_s$, $\beta_f = 150\mu_g(1 - \varepsilon_g)^2/d_s^2 \varepsilon_s$</p>
	gas–liquid	$\mathbf{F}_g^{l,d} = -\mathbf{F}_{l,d}^g = -\left(\frac{h_{l,d}}{d_l} + \frac{A_{sl,d}}{6}\right) \left[150\left(\frac{\varepsilon_s + h_{l,d}}{d_w}\right) \mu_g + 1.75\rho_g \mathbf{u}_g \right] \frac{\mathbf{u}_g}{\varepsilon_g}$
	solid–liquid	$\mathbf{F}_{l,d}^s = \left(\frac{150}{36} \mu_l \frac{A_{sl,d}^2}{h_{l,d}^2} + \frac{1.75}{6} \rho_l \frac{A_{sl,d}}{h_{l,d}} \mathbf{u}_l \right) \mathbf{u}_l$
Heat Transfer	gas–solid	$h_{gs} = \gamma Nu \lambda_g / d_s$, where $Nu = 2.0 + 0.6(Pr)^{0.333} (9Re)^{0.5}$
	gas–liquid iron	$h_{gl} = 4.18 \times 10^{-4} \varepsilon_g \rho_g \mathbf{u}_g c_{p,g} (\varepsilon_l \rho_l \mathbf{u}_l)^{0.35} Re_{gl}^{-0.37} (Sc/Pr)^{0.667} (T_l - T_g)$
	gas–slag	$h_{g-slag} = (0.203 Re^{0.33} Pr^{0.33} + 0.22 Re^{0.8} Pr^{0.4}) \lambda_g / d_s$
	solid–liquid	$h_{sl} = 1/(1/h_s + 1/h_l)$, where $h_s = 2\sqrt{\lambda_s c_{p,s} \rho_s \mathbf{u}_l - \mathbf{u}_s / \pi d_s}$, $h_l = 2\lambda_l / d_s \cdot \sqrt{Re_{sl} Pr_l} / (1.55\sqrt{Pr_l} + 3.09\sqrt{0.372 - 0.15Pr_l})$, $Re_{sl} = \phi_s d_s \rho_l \mathbf{u}_l - \mathbf{u}_s / \mu_l$, $Pr_l = c_{p,l} \mu_l / \lambda_l$
Heat Conductivity	gas	$\lambda_g = c_p \rho D_g^c$
	solid	$\lambda_{sc}^c = (1 - \varepsilon_g) / [(1/\lambda_s + 1/\lambda_s^c) + \varepsilon_g \lambda_s^c]$, where $\lambda_s^c = 2.29 \times 10^{-7} d_s T_s^3$
	liquid	$\lambda_l = 0.0158 T_l$

viscous fluid with no diffusion, and then the Navier–Stokes algorithm can be moderately modified to solve this flow. Liquid phase is treated as a mixture of slag and hot metal with average properties such as density and heat capability, based on their volume fractions. The force balance model^[31,32] considering gravity force, gas–liquid drag force and solid–liquid resistance force is used in the calculation of liquid flow and the corresponding velocity. Besides, energy and species transport equations are solved to obtain the temperature and component distribution of the three phases.

B. Inter-phase Momentum and Heat Transfer and Chemical Reactions

In this model, inter-phase mass, momentum and heat transfers are considered either as source or sink terms in the mass, momentum, and enthalpy balance equations for each phase. For gas–solid interactions, an Ergun-type equation^[33] is used to model the pressure drop in BFs. For gas–liquid and solid–liquid interactions, the liquid flow model proposed by Wang and Chew^[32] is adopted. The modified Ranz–Marshall equation^[34] is adopted in the calculation of heat transfer between the gas phase and solid phase. In the solution of heat transfer among the solid–liquid, gas–liquid iron and gas–slag phases, the Eckert–Drake equation,^[35] Mackey–Warner equation^[36] and Maldonado method^[37] are used, respectively. The details of those equations including the heat conductivity are listed in Table II.

The key chemical reactions considered in this model include the reduction of ferrous oxides (in the forms of hematite, magnetite, and wustite) by carbon monoxide and reduction of these ferrous oxides by hydrogen. One

interface unreacted shrinking core model is adopted for simulating these reduction reactions, which consider the gas film, diffusion and chemical reaction resistances. This model was proved to be sufficient and effective to model the reduction reactions of ferrous oxides in a BF.^[1,38] Also, the water-gas reaction, carbon solution reaction and direct reduction by carbon are considered. The detailed reactions and corresponding reaction rates included in this model are listed in Table III.

C. Cohesive Zone and Stagnant Zone

The cohesive zone is a key region in a BF where the solid iron ore is converted to liquid iron, and as a result, inside the cohesive zone, the porosity in the ore layers will be decreased and the density of softening ferrous oxides will be increased compared with burden ore layers. It is usually located between the lower part of the furnace shaft and the upper part of the furnace belly. In this region, solid ferrous oxides begin to soften and melt subject to material properties and thermal conditions. Usually, for a BF charged with a sinter of ordinary basicity, this region starts from ~ 1473 K and ends at ~ 1673 K. In this model, the cohesive zone is defined by solid temperatures between 1473 K and 1673 K, for example. Several methods were usually used in the treatment of the cohesive zone in previous BF mathematical models. In some works,^[10,19] regardless of the layered or non-layered structure of the cohesive zone, the void fraction of the cohesive layer was set as constant, such as 0.1. Second, the cohesive zone was treated as an anisotropic non-layered structure in some works,^[14] where coke and ore were treated as a mixture inside the cohesive zone and different vertical and

Table III. Key Chemical Reactions Considered in This Model

Chemical Reactions	Reaction Rate	Refs.
$\text{Fe}_2\text{O}_3 (s) + \text{CO} (g) = \text{Fe} (s) + \text{CO}_2 (g)$	$R_1^* = \frac{273 \cdot \pi d_{\text{ore}}^2 \varphi_{\text{ore}}^{-1} N_{\text{ore}} P (y_{\text{co}} - y_{\text{co}}^*) / (22.4 T_s)}{1/k_{f1} + (d_{\text{ore}}/2) [(1-f_s)^{-1/3} - 1] / D_1 + [(1-f_s)^{2/3} k_1 (1+1/K_1)^{-1}]}$	1,38
$\text{Fe}_2\text{O}_3 (s) + \text{H}_2 (g) = \text{Fe} (s) + \text{H}_2\text{O} (g)$	$R_2^* = \frac{273 \times \pi d_{\text{ore}}^2 \varphi_{\text{ore}}^{-1} N_{\text{ore}} P (y_{\text{H}_2} - y_{\text{H}_2}^*) / (22.4 T_s)}{1/k_{f2} + (d_{\text{ore}}/2) [(1-f_s)^{-1/3} - 1] / D_2 + [(1-f_s)^{2/3} k_2 (1+1/K_2)^{-1}]}$	1,38
$\text{C} (s) + \text{H}_2\text{O} (g) = \text{CO} (g) + \text{H}_2 (g)$	$R_3^* = \frac{273 \pi d_{\text{coke}}^2 \varphi_{\text{coke}}^{-1} N_{\text{coke}} P y_{\text{H}_2\text{O}} / (22.4 T_s)}{1/k_{f3} + 6 / (d_{\text{coke}} \rho_{\text{coke}} E_{f,w} k_3)}$	1,38
$\text{CO} (g) + \text{H}_2\text{O} (g) = \text{CO}_2 (g) + \text{H}_2 (g)$	$R_4^* = k_4 (V_{\text{ore}} / V_t) (1 - \varepsilon_g) \left(\frac{p}{0.082 T_s} \right) \left(y_{\text{co}} y_{\text{H}_2\text{O}} - \frac{y_{\text{co}_2} y_{\text{H}_2\text{O}}}{K_4} \right)$	1
$\text{C} (s) + \text{CO}_2 (g) = 2\text{CO} (g)$	$R_5^* = \frac{273 \cdot \pi d_{\text{coke}}^2 \varphi_{\text{coke}}^{-1} N_{\text{coke}} P y_{\text{CO}_2} / (22.4 T_s)}{1/k_{f5} + 6 / (d_{\text{coke}} \rho_{\text{coke}} E_{f,s} k_5)}$	1,38
$\text{FeO} (l) + \text{C} (s) = \text{Fe} (l) + \text{CO} (g)$	$R_6^* = k_6 (A_{\text{coke}} / V_t) \alpha_{\text{FeO}}$, where $A_{\text{coke}} / V_t = 0.078 [6(1 - \varepsilon_g) / (\varphi_{\text{coke}} d_{\text{coke}})]$	1,38
$\text{FeO} (s) = \text{FeO} (l)$ Flux (s) = Slag (l)	$R_7^* = \left\langle \frac{T_l - T_{\text{min,sm}}}{T_{\text{max,sm}} - T_{\text{min,sm}}} \right\rangle_0^1 \frac{\oint \omega_{\text{sm}} \mathbf{u}_i \rho_i \varepsilon_i dA}{M_{\text{sm}} V_{\text{ol,cell}}}$	10

horizontal drag resistances were employed. Third, the cohesive zone was treated with more details as in the studies^[12,39] where the different shrinkage stages of ore were considered, allowing for varying porosity, heat conduction and gas–solid heat transfers. In this article, the similar treatment for the layered cohesive zone is adopted considering the significant influence of cohesive zone treatment on BF thermal and chemical efficiency. Moreover, in this model, the layer thickness variation in the cohesive zone caused by ore melting is not explicitly considered for simplification. It is implicitly considered by means of considering the effects of the shrinkage index on the calculations of gas flow resistance, heat exchange between gas and solid materials, and solid heat conductivity in the region of the cohesive zone; as a result, for example, the porosity of ore layer will be reduced in the simulation results. This treatment has been widely used in many recent papers on BF modelling^[12,24,26,39] and has been proved effective to capture the flow-thermal state around the cohesive zone. The detailed treatment of the cohesive zone including three different shrinkage stages was detailed elsewhere^[12,39] and is not included here for brevity.

In the stagnant region (deadman) and dripping zone, it is assumed that only coke exists in solid state. The coke bed permeability in the dripping zone is set according to the coke size distribution extracted from the stockline. However, for the treatment of permeability in the stagnant region, a constant coke size (25 mm) and porosity (0.65) are used. The outer boundary of the stagnant region is determined using an iso-velocity curve of coke particles at a critical value—one ninth the particle diameter per minute.^[40] Once the boundary is determined, the coke particles will be set as motionless inside this region.

D. Layered Structure of Burden with Respective Chemical Reactions

Instead of solving solid flow using potential flow theory as reported in the previous works,^[15,19] in this work, the solid velocity field and streamline are calculated based on the viscous model. Then, the timeline can be solved based on the equations listed below.

$$\Delta t = \frac{L_s}{u_s} \quad [1]$$

$$t_{\text{time}} = \sum_i \Delta t_i \quad [2]$$

where L_s (m) is the distance of two adjacent nodes along the streamline, u_s is the particle velocity magnitude (m/s), and t_{time} (s) represents the time needed for a downward-flowing solid particle to reach a specified location.

The coke and ore burden descending time through the stockline could be obtained by the hot metal productivity and batch weight as follows.

$$t_d = \frac{24 \times 3.6 W_{\text{batch}}}{P V_{\text{bf}} (\lambda_{\text{coke}} + \lambda_{\text{ore}} + \lambda_{\text{flux}})} \quad [3]$$

where W_{batch} (kg) is the total batch weight of coke, ore and flux; P and V_{bf} are the productivity ($\text{t/m}^3 \text{d}$) and furnace volume (m^3), respectively. λ_{coke} , λ_{ore} and λ_{flux} are the coke, ore and flux ratio, respectively.

The time needed for coke (t_{coke}) and ore (t_{ore}) particles to pass through the stockline could be solved according to their volume fractions as follows.

$$t_{\text{coke}} = t_d \times V_{f_{\text{coke}}} \quad [4]$$

$$t_{\text{ore}} = t_d \times V_{f_{\text{ore}}} \quad [5]$$

where $V_{f_{\text{coke}}}$ and $V_{f_{\text{ore}}}$ are the volume fractions of coke and ore along the radial direction, respectively. Note that the flux volume is neglected here for simplicity. Assuming the hot meal production rate and charging pattern are fixed, the descending time for each batch is constant. Based on the timeline calculation results, the total number of batches above a specified position and the determination of coke layers and ore layers could be achieved using the following expressions for the case of charging ore first.

$$N_{\text{batch}} = \text{int} \left(\frac{t_{\text{time}} + t_{\text{ore}}}{t_d} \right) - \text{int} \left(\frac{t_{\text{time}}}{t_d} \right) \quad [6]$$

where N_{batch} is the logical variable in the layered structure determination. When its value is equal to zero, the layer will be regarded as the coke layer. Otherwise, it will be ore layer. Each layer then will be set with the corresponding properties, such as heat capacity and density, as well as a logical reaction switch. Specifically, the ore-related reactions such as the hematite reduction by carbon monoxide and hydrogen are set to take place in the ferrous oxide layers, while the carbon solution reaction happens in the coke layer only. The reaction of gas–water is treated as taking place in both the ore and coke layers.

In this model, one interface unreacted shrinking core model is adopted in the calculation of ferrous oxide reduction. The reduction of ferrous oxides is considered a process of oxygen element transfer from iron-bearing ore to reducing gas. The oxygen element is gradually captured by, for example, CO and H₂. Thus, the molar ratio of the O to Fe element in ferrous oxides gradually changes. In this article, the reduction degree is calculated based on the following expression.

$$R_{\text{ore}} = 1 - \frac{2 n_{\text{O}}}{3 n_{\text{Fe}}} \quad [7]$$

where n_{O} is the residual mole of oxygen element in ore, and n_{Fe} is the total mole of iron element. If the ore is in the form of hematite only, the reduction degree is zero; if the ore is magnetite only, the reduction degree is one ninth, and so on. The reduction degree changes as ferrous oxide reduction continues.

In this model, the moles of O and Fe elements in ferrous oxides are calculated in the simulation, and thus the forms of ferrous oxides in different reduction stages can be derived based on the O/Fe ratio or oxide reduction degree. Plus, considering the following molar balance equation of the O and Fe element, the mass fraction of different ferrous oxides (hematite, magnetite, wustite and metal iron) can be achieved.

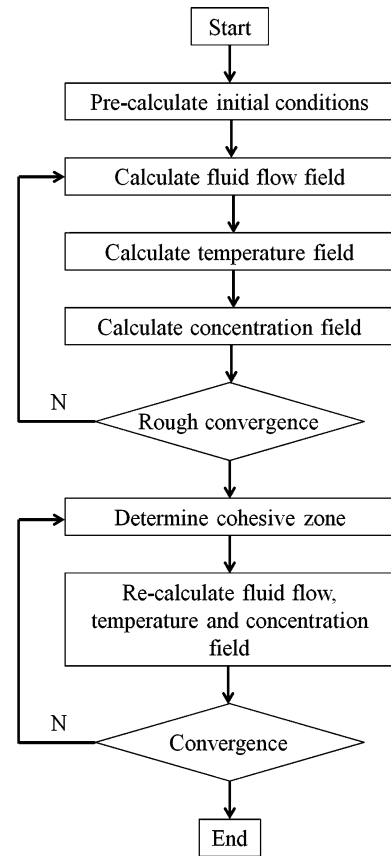


Fig. 2—Schematic of the solution procedure of the BF model.

$$\sum_i \text{Fe}_i = n_{\text{Fe}} \quad [8]$$

$$\sum_i \text{O}_i = n_{\text{O}} \quad [9]$$

where Fe_i and O_i are moles of Fe and O of different ferrous oxides in the respective reduction stage, respectively.

E. Solution Algorithms and Convergence

The flowchart of the solution procedure is shown in Figure 2. Variable initialization is carried out first. Then, some basic calculations, for example reducing the gas components and their temperatures are solved based on mass and material balance models. The flow field will be calculated to provide a relatively good precondition for the temperature field. When the basic distributions of multiphase flow and temperature are achieved, components in the gas and solid phases will be solved where notably chemical reactions will take place in their corresponding layers. After this rough

convergence, the cohesive zone can be determined based on solid temperature subject to iron ore properties; for example, in this study 1473 K to 1673 K is used. Then, another loop considering the existence of cohesive zone is used to obtain the final converged results. Notably, coke combustion in the raceway is considered implicitly through the pre-calculated material balance and energy balance in this model. These calculations can provide boundary conditions to the subsequent BF model including the reducing gas component and temperature. The raceway is also treated as a solid exit in this model. This treatment has been commonly adopted in many published works.^[10,12,13,16–19,24,26]

In this BF process model, the position of the cohesive zone is used as one of convergence criteria, as used in References 14 and 39. In addition to the cohesive zone position, the gas utilization ratio of both carbon monoxide and hydrogen is also used as an additional convergence criterion. The expression of this criterion is written as follows.

$$\text{sqrt} \left(\sum_{i=n+1}^i \left(\chi_i - \sum_{i=n+1}^i \chi_i / n \right)^2 / n \right) \leq \bar{\epsilon} \quad [10]$$

where χ_i is the gas utilization ratio at the furnace top for carbon monoxide and hydrogen, respectively; i , n and $\bar{\epsilon}$ are the array index of the gas utilization ratio, count number of gas utilization data and convergence criteria, respectively. In this model, the gas utilization ratio is monitored after each loop, n is set to 100. $\bar{\epsilon}$ of, and CO and H₂ are set as 0.5 and 1.0, respectively. This convergence criterion is a more convenient measure of convergence and can be used in future BF model studies.

III. SIMULATION CONDITIONS

The operational data of a BF in real practice are used as boundary conditions in this study. A non-orthogonal body-fitted method is adopted in meshing. Structured mesh with a relatively regular node distance is prepared for better tracking of solid movement and minimizing calculation error. The computational domain and mesh near furnace top are shown in Figure 3. The key operational parameters of the BF are listed in Table IV.

IV. RESULTS AND DISCUSSION

A. Typical Results

1. Cohesive zone

Figure 4 shows the cohesive zone (CZ) coloured by different shrinkage stages^[12,39] (shrinkage index). For the better understanding and presentation of the cohesive zone structure, a 3D contour (see Figure 4(b)) based on the 2D axial calculation result is plotted. An inverse-V-shaped CZ is clearly seen inside a BF. The pre-set charging pattern is the main cause for a specific CZ pattern. Also, the thickness of CZ was observed to

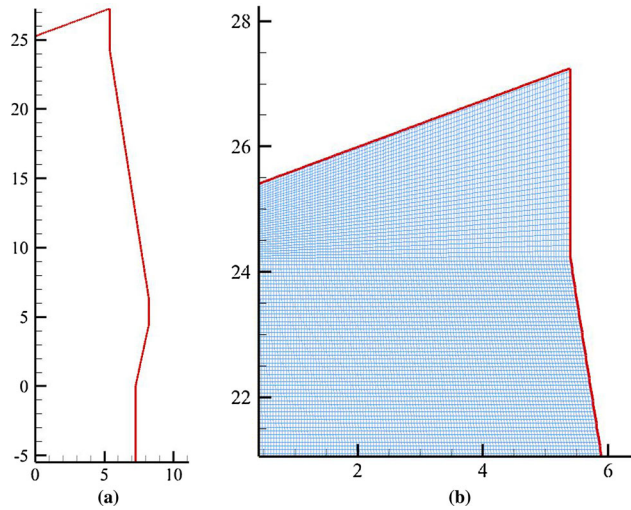


Fig. 3—Computational domain (a) and mesh near the top of the BF (b).

vary with its distance from the furnace wall. As seen in Figure 4, the piled cookie-like layers of the softening ore show lower gas permeability. As a result, reducing gas will flow through the low-resistance coke windows between two adjacent ore layers.

2. Flow pattern

Figure 5 shows the distribution of gas velocity, gas density, solid velocity and solid density simulated by this model, respectively. Figure 5(a) gives the detailed information of the gas flow field. At the lower part of the BF, the gas velocity is relatively higher near the tuyere since gas flow is accelerated through the tuyere. Then, gas flows toward to furnace centre and furnace top. Due to different local porosities and particle diameters, different flow patterns can be observed in different regions. For example, around the region of the cohesive zone, gas prefers to flow directly through the coke windows rather than ore layers because of the higher resistance of the latter than the former. The densities of both gas and solid are important variables as they will play an indispensable role in the subsequent heat transfer. Figure 5(b) shows the gas mixture density. It is noted that the density of the gas mixture at the lower regions is much smaller than that at the upper regions. This reflects that the temperature may override the pressure in the density calculation, considering the lower region is a high-temperature and at the same time a high-pressure region where the temperature and pressure will act oppositely in the density calculation. Figure 5(c) shows the velocity field of the solid phase predicted by this model. In this model, the solid phase including coke and ore particles is charged alternatively from the furnace top. Then, they flow downward along the streamline toward the raceway, which is treated as a solid exit. Coke inside the stagnant region is considered motionless in this model and behaves as the boundary for solid flow. Figure 5(d) illustrates the density distribution of the solid phase with a layered charging pattern. It is observed that the ore density in the cohesive zone

Table IV. Operational Parameters and Simulation Conditions in This Model

Parameters	Values
Gas	
Blast Volume Flux (Nm ³ /tHM)	1140
Blast Temperature (K)	1473
Oxygen Enrichment (pct)	1.7
Moisture (g/Nm ³)	8.036
Top Gas Pressure (atm)	2
Reducing Gas Volume (Nm ³ /tHM)	1437
Reducing Gas Components (pct)	CO 35.60; N ₂ 59.47; H ₂ 2.0; H ₂ O 0.0; CO ₂ 0.0
Solid	
Ore Rate (t/tHM)	1.597
Average Ore Components (pct)	TFe 59.93
Coke Rate (t/tHM)	0.343
Coke Main Components (pct)	C 86.794; Ash 12.162; S 0.594
Coal Rate (t/tHM)	0.17
Coal Main Components (pct)	C 75.3; Ash 14.78; S 0.36
Flux Rate (t/tHM)	0.089
Flux Main Components (pct)	Gangue SiO ₂ 92.37 Limestone CaO 54.93; CO ₂ 43.06 Dolomite CaO 32.38; MgO 19.95; CO ₂ 45.42
Solid Inlet Temperature (K)	300
Coke Volume Fraction (—)	0.153 log d_{coke} + 0.724
Ore Volume Fraction (—)	0.403(100 d_{ore}) ^{0.14}
Average Coke Particle Diameter (m)	0.045
Average Ore Particle Diameter (m)	0.03
Hot Metal	
Productivity (t/m ³ d)	2.0
Main Components (pct)	Fe 95.369; C 3.805
Density (kg/m ³)	6600
Viscosity (kg/m s)	0.005
Conductivity (W/m K)	28.44
Surface Tension (N/m)	1.1
Slag	
Slag Rate (t/tHM)	0.323
Slag Main Components (pct)	CaO 39.55; SiO ₂ 33.57; FeO 0.36
Basicity (—)	B_2 1.178; B_3 1.412; B_4 0.982
Density (kg/m ³)	2600
Viscosity (kg/m s)	1.0
Conductivity (W/m K)	0.57
Surface Tension (N/m)	0.47

increases because of the softening process. In the dripping and stagnant zone, only coke exists in the solid phase, maintaining its density as upper BF regions.

3. Temperature distributions

The simulation results of temperature fields of the gas, solid and liquid phases are shown in Figure 6. The temperatures of the gas, solid and liquid phases are all relatively higher around the raceway than in the other BF regions because of the intense combustion between the hot blast and coke near the raceway. Due to the temperature difference between the gas and solid and/or gas and liquid in this region, the solid and liquid are heated up quickly. Beyond the raceway region, the temperatures of the gas, solid and liquid are all higher near the centre than near the wall along the radial direction because of higher permeability at the furnace centre caused by the pre-set charging pattern, allowing a high-temperature gas pass through the central part

easily with more energy. The effect of the layered structure on temperature is considered by means of calculating the temperature field of both the gas and solid phase using different solid properties in different layers, for example, the particle size, shape factor, density, heat capability and heat conductivity, although only one solid temperature equation is used. This effect is reflected and evidenced by the fluctuating iso-lines of the solid temperature (Figure 6(b)). A similar treatment was used in BF modelling works.^[13,20–22,24,26,39] Along the longitudinal direction, both the gas and solid phases have three different temperature regions. The first region is below the cohesive zone, where both the gas and solid temperature decrease sharply, mainly because of the direct endothermic reduction, carbon solution and liquid formation taking place there. The second temperature region is the one primarily across most of the furnace shaft. The temperature in this region shows relatively smooth variations compared with that of the

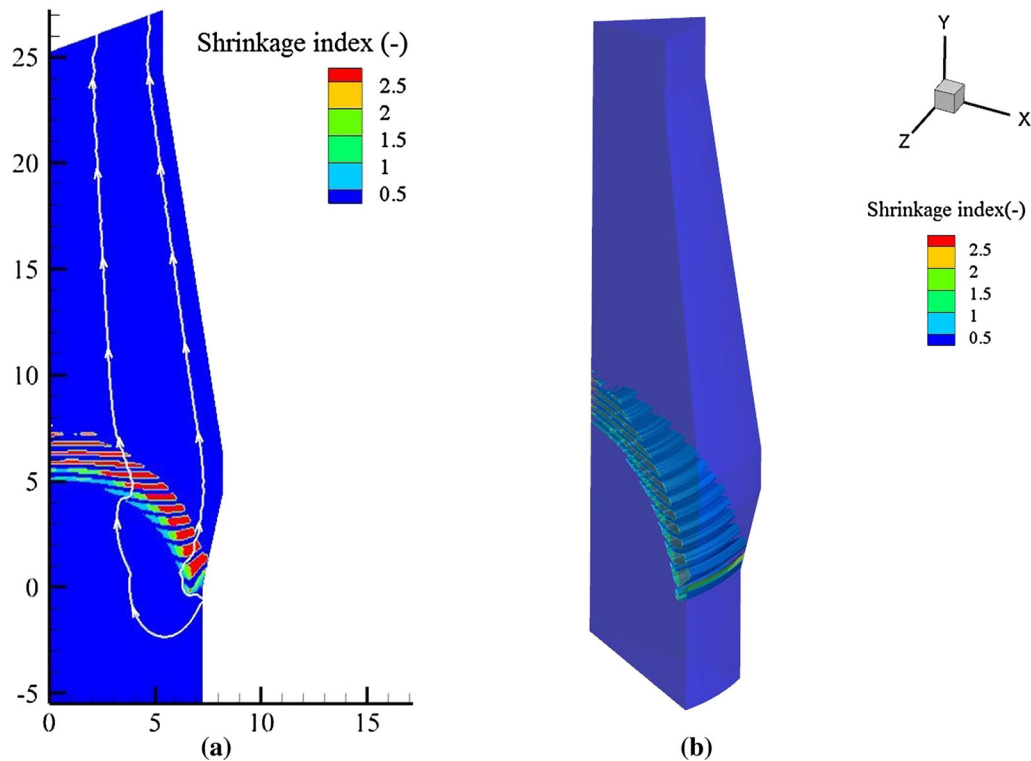


Fig. 4—Cohesive zone in BF: (a) 2D and (b) 3D.

first region. The main chemical reactions of ferrous oxides in this region are indirect reductions by CO and H₂. This region is also called the thermal reserved zone, where the heat exchange rate between the gas and solid phase is quite slow (Figure 6(d)) resulting from their similar water equivalent.^[41] The third region is near the furnace top, approximately above the 800 K isothermal line. In this region, both the gas and solid phases show rapid variation of temperature mainly because of the intense convective heat flow. In addition, the temperature difference between the gas and solid phase is shown in Figure 6(d), where the isothermal lines with labels are the gas temperature for comparison. It is observed that the difference value or (*D* value) of temperature reaches its peak near the raceway and it stays relatively stable along most of the furnace shaft. Moreover, there are two zones with relatively larger *D* values around the cohesive zone and near the furnace top, respectively, compared with the shaft due to the large water equivalent difference between the gas and solid phase, which is affected by strong local endothermic chemical reactions such as a direct reduction in and around the cohesive zone and the exothermic reaction of indirect reduction by CO near the furnace top, respectively.

4. Components of gas and solid phases

Figure 7 shows the simulation results of the mole fractions of CO and CO₂ inside the BF. In Figure 7(a), as a whole, the concentration of CO continually decreases when gas flows toward the furnace top because of the indirect reduction, except for the region

adjacent to the lower cohesive zone, because of the direct reduction of wustite by coke particles in this region, producing extra CO compared with that in the raceway. On the other hand, the CO₂ mole fraction in Figure 7(b) shows a reversing distribution compared with that of CO in Figure 7(a), namely, increasing gradually along the gas streamline, because CO and CO₂ are reactant and product, respectively, in the indirect reduction of ferrous oxides. The concentrations of CO and CO₂ near the furnace central line are both higher than that near the wall, because the central gas flow is better developed compared with peripheral gas because of the porosity difference. Specifically, in the middle upper region of the furnace shaft, the contours become denser for both CO and CO₂ compared with the upper regions, indicating a sharp CO decrease and CO₂ increase due to the indirect reduction and water-gas reactions. In addition, there are sharp angles in the middle regions near the furnace wall in both contours, indicating the transformation from CO to CO₂ by the water-gas shift reaction. More importantly, both contours demonstrate the concentration fluctuations, especially in the upper shaft due to the unique treatment of the layered reacting structure in this model, where the reduction of ferrous oxides only takes place in their own layers, leading to the fluctuating iso-lines. This is one of the significant features in this BF model.

Figure 8 presents the concentration distribution of H₂ and H₂O. Similar to the relationship between CO and CO₂, the concentrations of H₂ and H₂O show opposite profiles. This is because H₂ is one of the reactants that

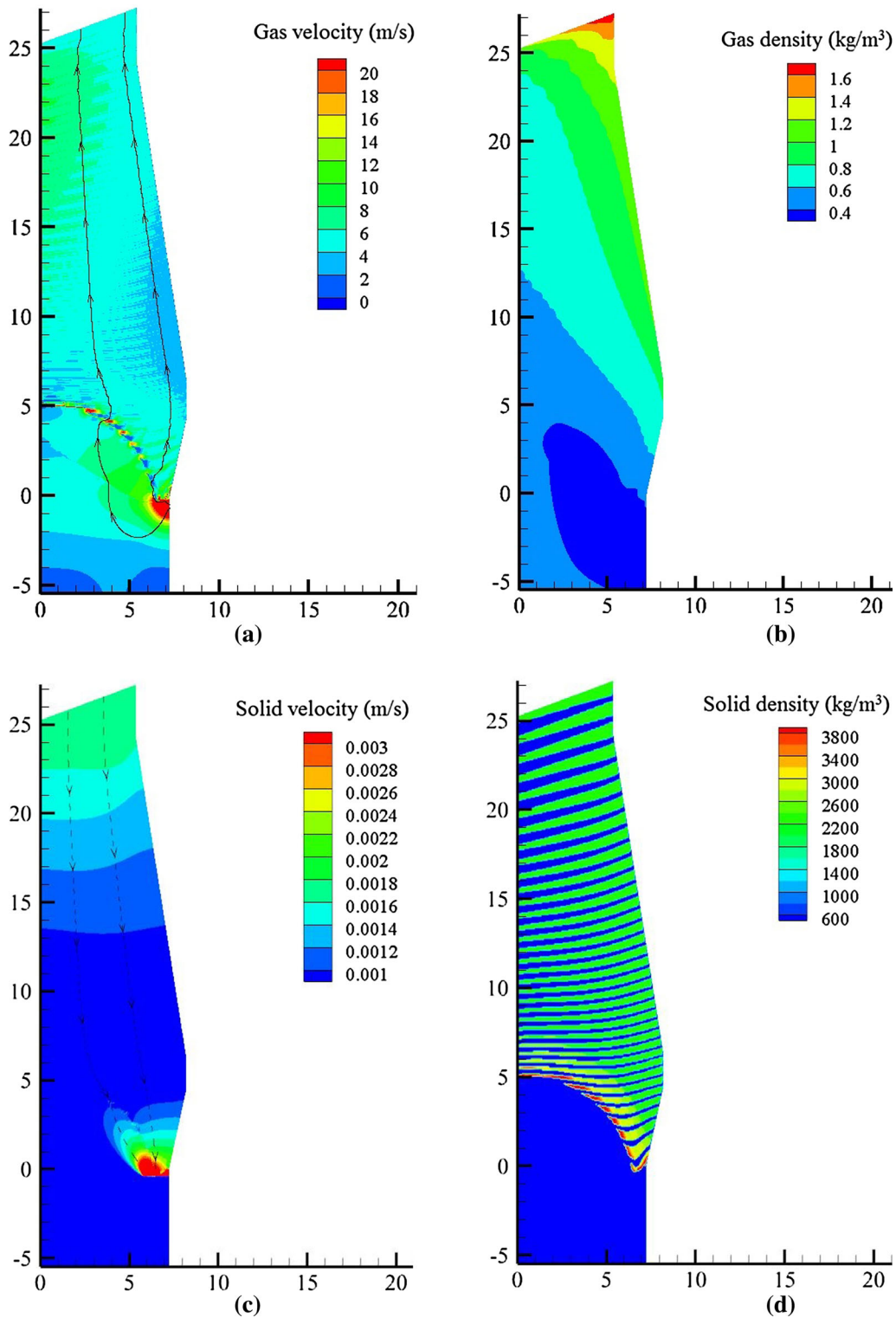


Fig. 5—Typical flow phenomena: (a) gas phase velocity; (b) gas phase density; (c) solid phase velocity; (d) solid phase density.

will combine with the oxygen element existing in ferrous oxides while H₂O is one of the final products. A relatively higher H₂ concentration is observed in the lower region, as shown in Figure 8(a). This is because water vapour from the humidified blast will be

decomposed to H₂ and CO when coming into contact with hot coke. Then, the H₂ will expand to other areas with its concentration level decreasing in the gas mixture. It is also observed that both concentrations show sudden changes in the middle-lower region of the

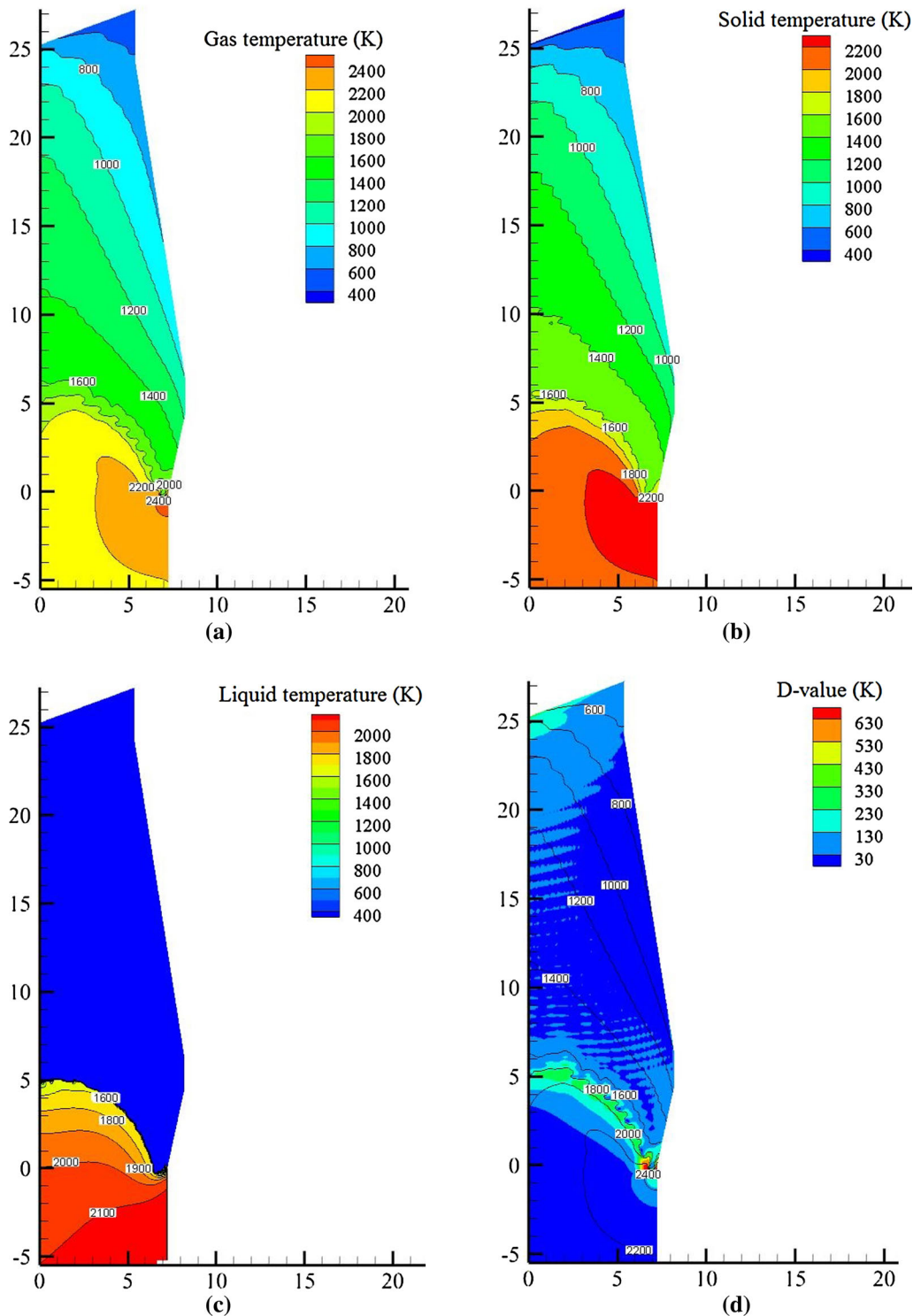


Fig. 6—Temperature fields: (a) gas phase; (b) solid phase; (c) liquid phase; (d) temperature difference between gas and solid phase.

furnace shaft, because ferrous oxide reduction by H_2 prefers to take place in high-temperature regions, and the contours of both H_2 and H_2O become quite dense compared with that in other areas. In addition, the fluctuating iso-lines and sharp angles are captured in both contours, the reason being the same as those for CO and CO_2 . Water evaporation in the shaft is not considered in this model for simplicity.

Figure 9 shows the mass fraction distributions of hematite, magnetite, wustite and metal iron inside the BF. In this figure, the plotted lines and their values represent the solid temperature. They are given here for quick determination and comparison of the temperature range where those four materials are present. Figures 9(a) to 9(c) shows that hematite, magnetite and wustite have their corresponding chemical reserve

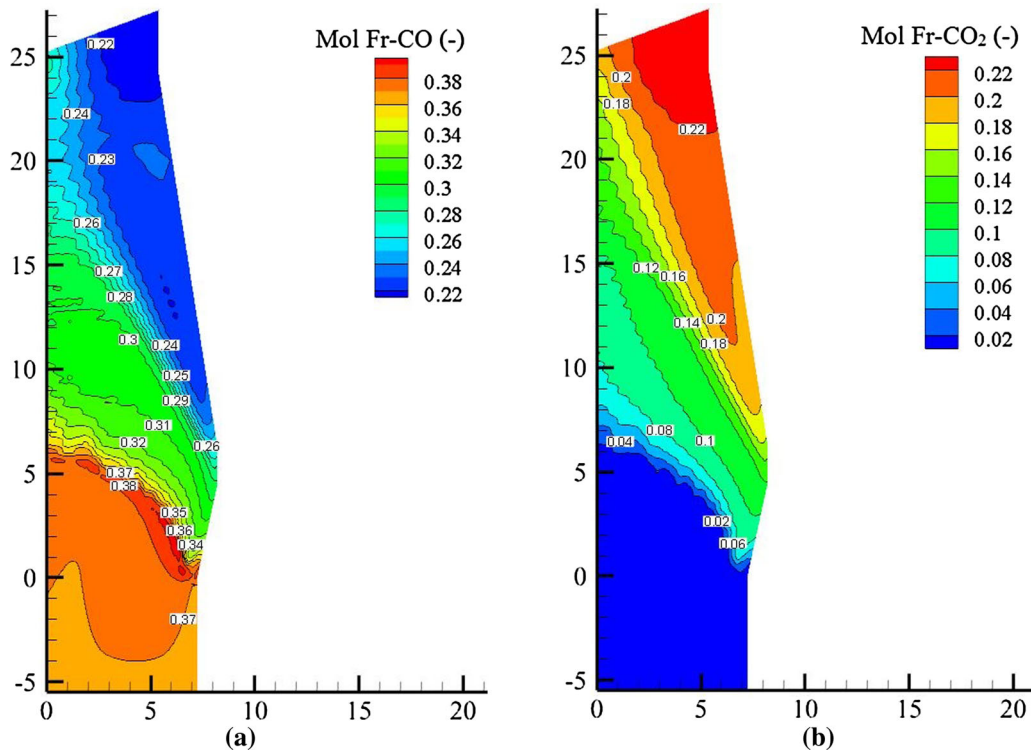


Fig. 7—Concentration fields of CO (a) and CO₂ (b).

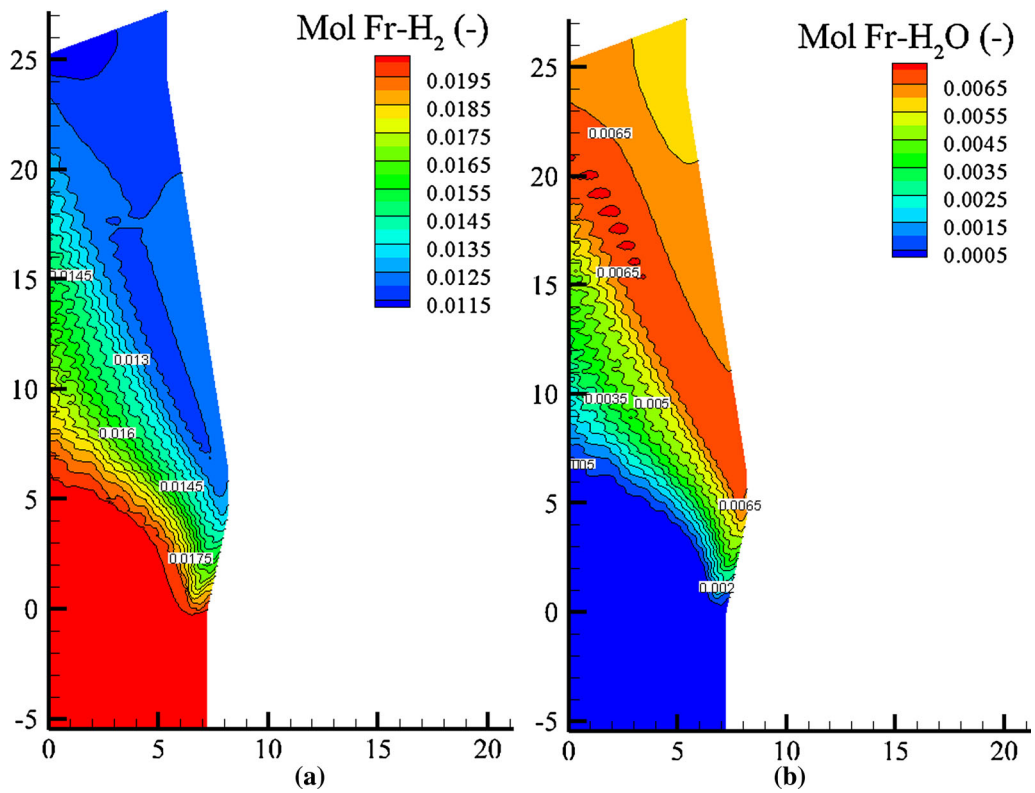


Fig. 8—Concentration fields of H₂ (a) and H₂O (b).

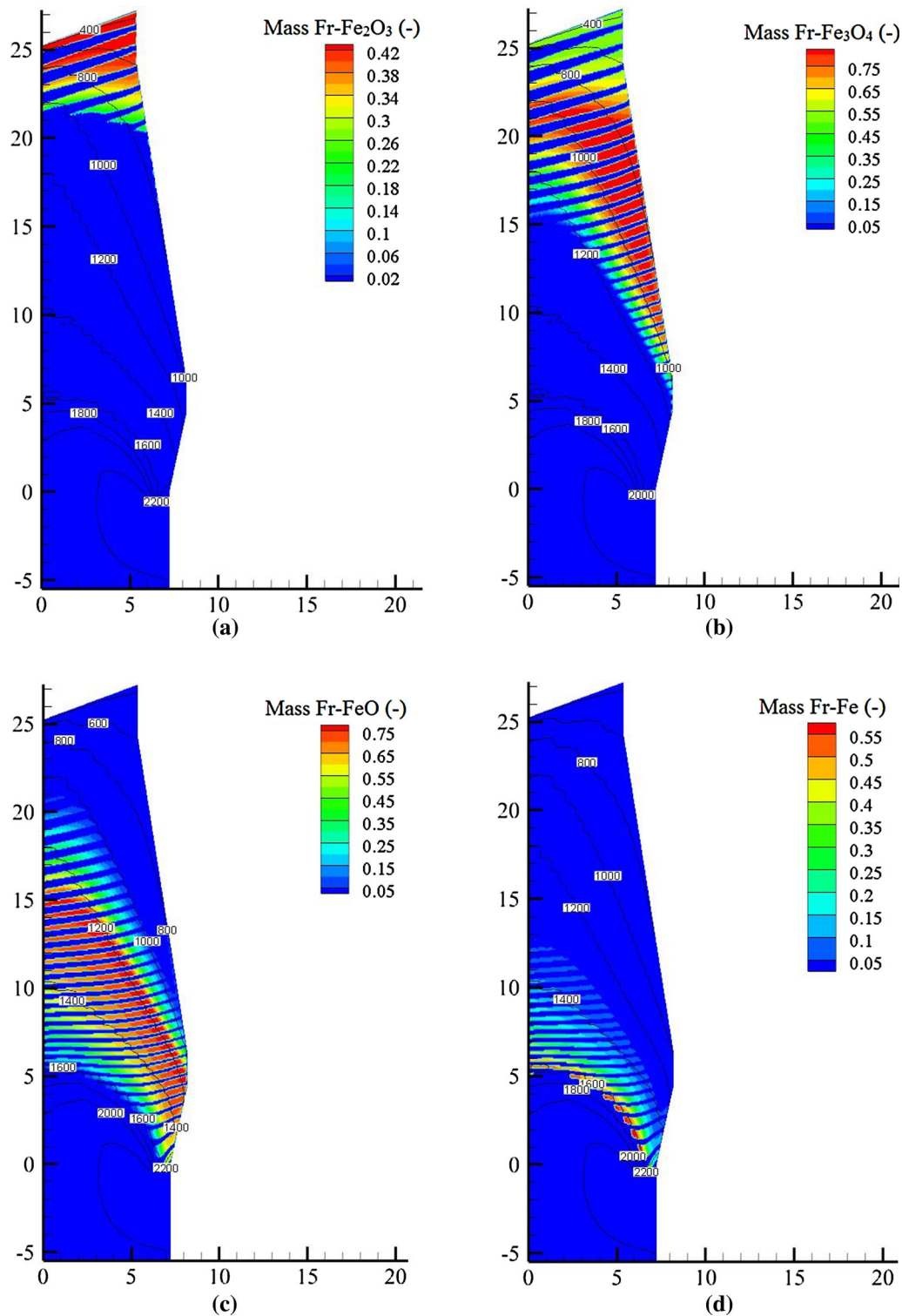


Fig. 9—Distribution of solid component mass fraction: (a) hematite; (b) magnetite; (c) wustite; (d) metal iron.

zone, respectively, that is, its mass fraction will stay constantly high in the corresponding chemical reserve zones, as coloured in red.

To be specific, Figure 9(a) indicates that the hematite level stays constantly high near the stockline level. This is because the reaction rate of hematite is insignificant, and the thermodynamic equilibrium constant is small

under the local low-temperature conditions. When hematite moves downward and reaches a relatively higher temperature zone of 800 K, its mass fraction will decrease significantly. Below this level, magnetite begins to form and only a small percentage of hematite is left in the ore layers. This distribution of hematite is similar to some previous works.^[19,42] Figure 9(b) indicates that

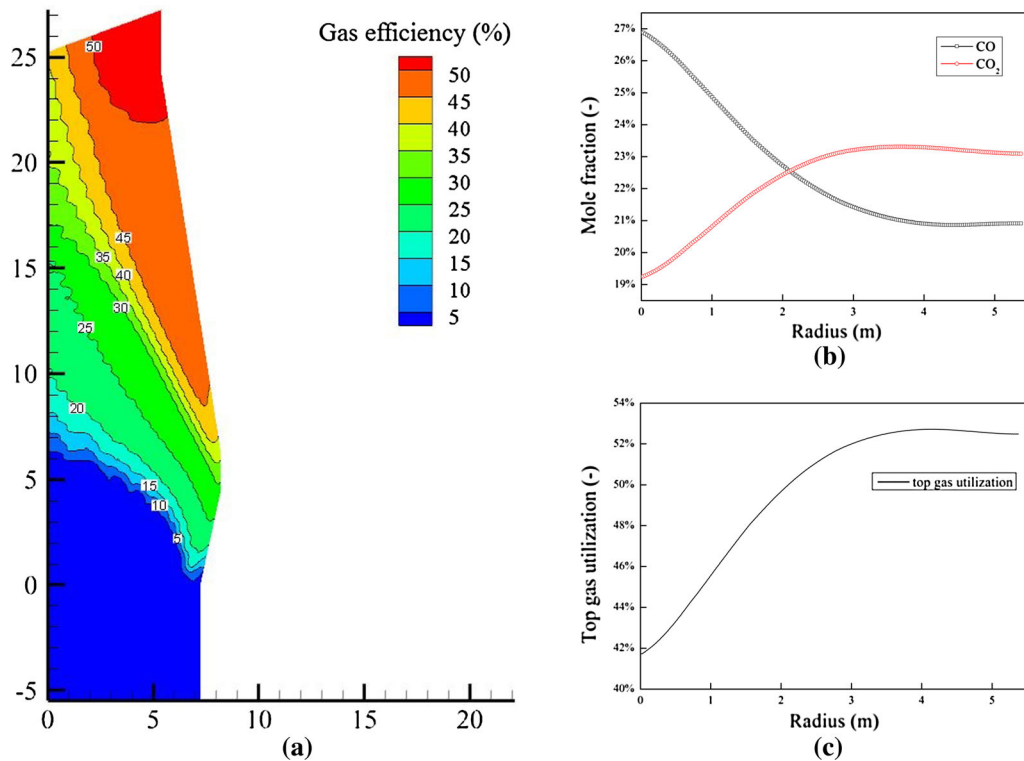


Fig. 10—Gas species-related information: (a) gas utilization efficiency through the whole domain of BF; (b) distribution of CO and CO₂ along the top surface; (c) top gas utilization efficiency along the radial direction.

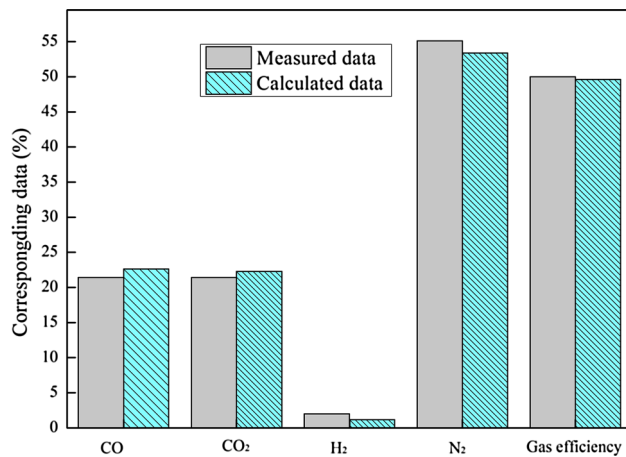


Fig. 11—Comparison between measured and calculated data of top gas information.

some magnetite is found near the furnace top, as magnetite is charged into BF with hematite, that is, both of them are the main components of ferrous oxides in the charged ore. In the low temperature region, magnetite is stable since the decomposing condition has not been reached. Then, the mass fraction of magnetite grows substantially and reaches its peak at roughly the temperature of 900 K. This is because it is the step-by-step transformation from hematite to magnetite. Specifically, after all hematite has been reduced to magnetite,

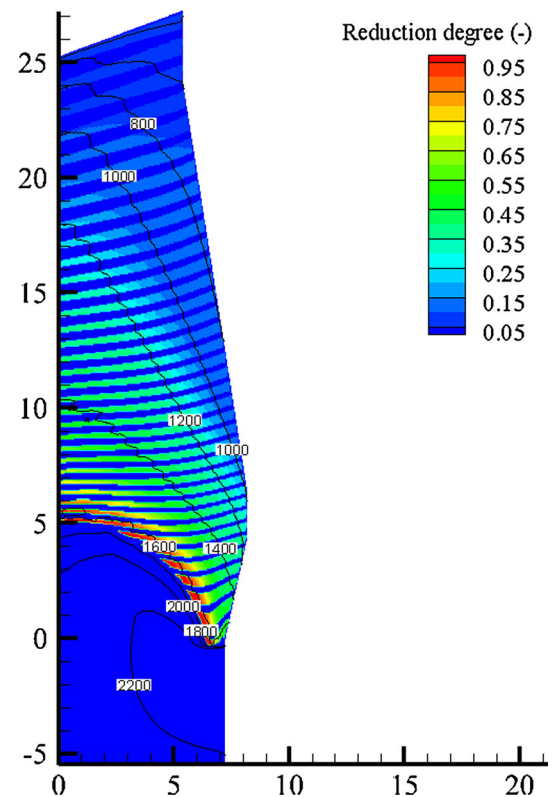


Fig. 12—Reduction degree of ferrous oxides.

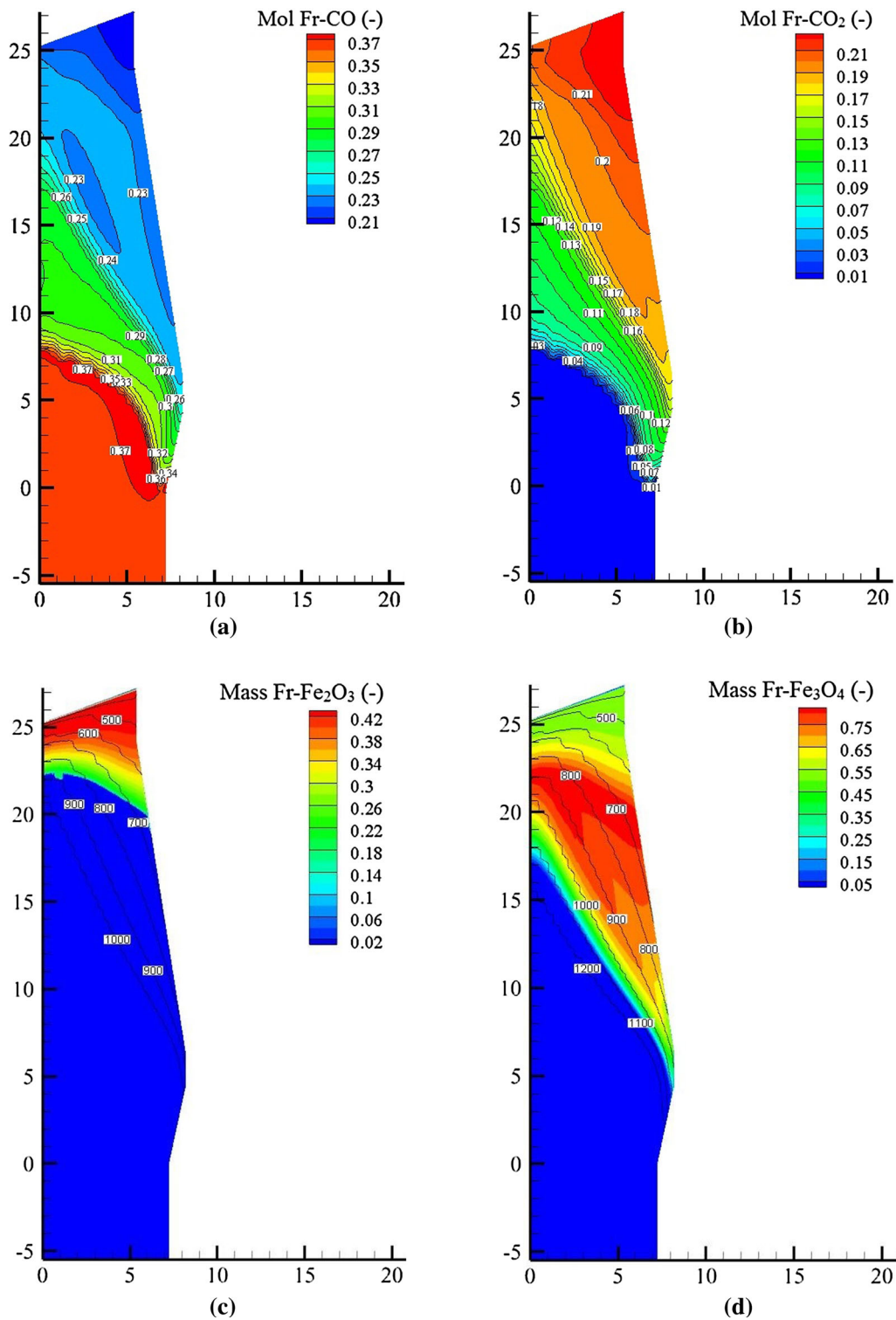


Fig. 13—Distribution of molar fraction of gas components: (a) CO; (b) CO₂; mass fraction of ferrous oxides: (c) Fe₂O₃ and (d) Fe₃O₄ calculated by a model with non-respective chemical reactions in burden layers.

the mass fraction of magnetite would stay almost unchanged through the upper shaft near the wall. Thus, the chemical reserve zone of magnetite is formed, since the reduction from magnetite to wustite has not started yet. Also, its location matches the region of loose iso-lines of the gas concentration distribution (Figures 7

and 8). When the reducing conditions including the gas concentration, partial pressure and phase temperature are satisfied (roughly ranging from 1000 K to 1200 K), magnetite will begin to be reduced to wustite, as shown in Figure 9(b). Figure 9(c) indicates that wustite shows a similar tendency as that of magnetite. First, wustite is

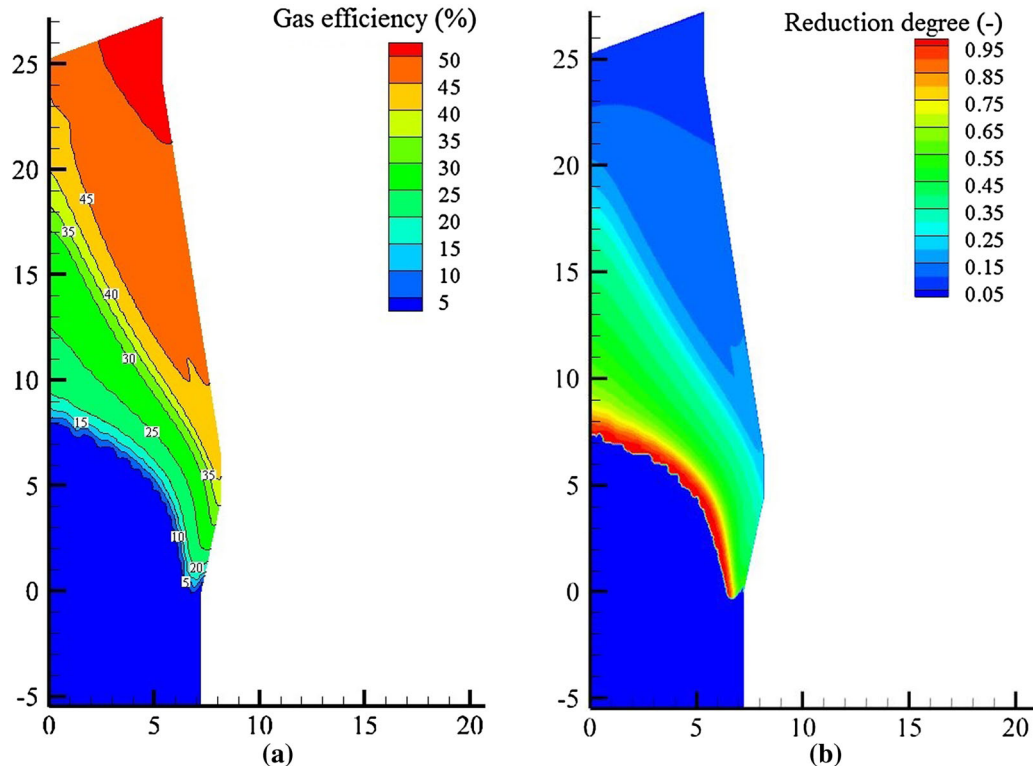


Fig. 14—Distribution of: (a) gas utilization efficiency and (b) ferrous oxide reduction degree simulated by a model with non-respective chemical reactions in burden layers.

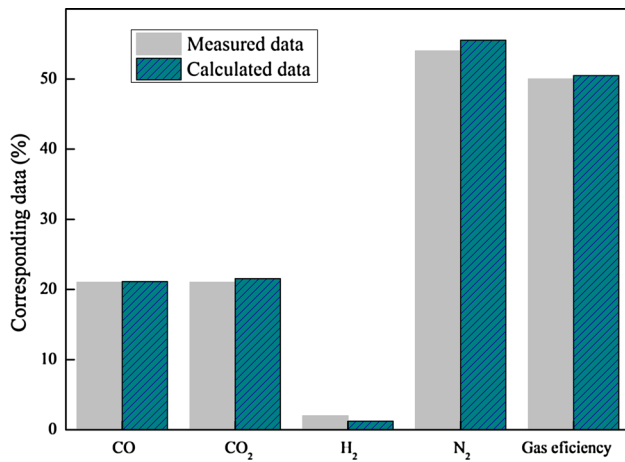


Fig. 15—Comparison of top gas information between measured data and model-simulating results.

produced in the further reduction of ferrous oxides, namely reducing gas consumes more oxygen element from magnetite. The highest level of wustite in ferrous oxides is roughly around 1300 K. Then, its level drops because of the continued reduction from wustite to metal iron. Unlike magnetite, wustite prefers to be reduced quickly after reaching its maximum mass fraction, indicating a good reduction environment near the lower part of the wustite reserve zone. Finally, Figure 9(d) shows that metal iron is quickly generated near the solid temperature 1600 K (namely the lower

boundary of the cohesive zone). It is a higher level near the furnace centre but a lower one near the furnace wall because the higher permeability is located near the furnace centre, representing a higher reducing potential in this region. Metal iron increases as wustite decreases, as shown in Figures 9(c) and 9(d), reflecting the successive reduction of ferrous oxides. The contour also shows the metal iron mass fraction is increased rapidly with the increase of temperature, especially in the temperature range of the cohesive zone, indicating the acceleration of the reduction progress. This reduction characteristic could also be reflected in the dense iso-lines of the gas concentration as shown in Figures 7 and 8. Notably, the alternative layered structure in these reserved zones with fluctuating temperature iso-lines can be captured by this model. They cannot be well captured in the previous BF model considering the respective reacting burden layers.^[13] This is also a significant feature in this BF model.

B. Furnace Performance

1. Gas utilization

Figure 10 shows the gas utilization efficiency through the whole domain of BF, mole fractions of CO and CO₂ and gas utilization at the furnace top, respectively. Top gas efficiency is one of the important smelting indexes in actual BF operations. Since top gas is yielded from reducing gas, to some extent, it could reflect the BF performance and also the inner situations of the BF. The gas utilization efficiency is defined as follows.

$$\chi = \frac{(\text{CO}_2)_{\text{pct}}}{(\text{CO})_{\text{pct}} + (\text{CO}_2)_{\text{pct}}} \quad [11]$$

Figure 10(a) shows that gas efficiency evolves from the tuyere level up to the furnace top. Since hot coke particles are packed below the cohesive zone, almost no CO_2 could stay after the carbon solution reaction. As a result, the gas utilization efficiency is quite low in this region. The fluctuating iso-lines are also observed for gas utilization efficiency because of the layered reacting structure considered in this model. Then, from the cohesive zone to furnace top, gas efficiency evolves slowly from 20 to 30 and 45 to 50 pct, respectively. These regions match the chemical reserve zones of wustite, magnetite and hematite, respectively (Figure 9).

Figure 11 compares the top gas efficiency obtained from the measurements and simulation subjected to the simulation conditions listed in Table IV. Note that the unit in this figure is the volumetric fraction, and the mean value of each component is plotted and compared. The mean top gas efficiency is defined as follows.

$$\bar{\chi} = \frac{\sum (\text{CO}_2)_{\text{pct}}}{\sum (\text{CO})_{\text{pct}} + \sum (\text{CO}_2)_{\text{pct}}} \quad [12]$$

It is indicated that the simulation results of gas concentrations of CO , CO_2 , H_2 and N_2 agree well with the measurements, confirming the validity and effectiveness of this mathematical model.

2. Reduction degree

Figure 12 shows the reduction degree of solid ferrous oxides in the BF. Note that only the reduction degree of ferrous oxides above the dripping zone is presented in this contour map. Since coke and ore are charged layer by layer and the coke-ore mixture is neglected in this model, there is no penetrating ore particle in coke layers. The iso-lines of the solid temperature are also plotted in Figure 12. From the top to tuyere level, the reduction degree in ore layers gradually increases to 100 pct. The increasing tendency of the reduction degree corresponds to the distribution of various ferrous oxides. In particular, the reduction degree in chemical reserve zones of hematite, magnetite and wustite shows little growth compared with that in other regions because of the reserve effect, as stated before. Besides, the reduction degree is much higher at the furnace centre than that near the wall, indicating the much faster reduction happens at the centre because of the well-developed central gas.

3. Comparison between BF models with vs. without respective chemical reactions in coke and ore burden layers

To demonstrate the effectiveness of considering the respective chemical reactions in coke and ore layers, the results simulated by a model with the layered burden structure but without considering respective chemical reactions are presented in Figures 13 to 15. They are compared with the above-mentioned simulation results using the model with respective chemical reactions under the same boundary conditions.

Figure 13 presents the molar fractions of CO , CO_2 and the mass fractions of Fe_2O_3 and Fe_3O_4 , respectively. Both models show similar distributions of gas species. Specifically, the dense iso-lines caused by rapid chemical reactions indicate the quick change in gas species. However, the profiles of iso-lines in Figure 13 are much smoother than those in Figures 7 and 8, that is, the model without respective reacting structure fails to capture the fluctuating iso-lines of the gas components. On the other hand, the mass fractions of solid components show non-fluctuating distribution across the furnace shaft due to the fact that the layered burden structure is not applied.

The gas utilization efficiency and solid ferrous oxide reduction degree of the model without respective chemical reactions are also plotted in Figure 14 for comparison. Both models show similar distributions of gas utilization efficiency and ferrous oxide reduction degree. However, the iso-lines of gas utilization in the model of this section are quite smooth with few fluctuations due to the omission of respective chemical reactions in alternative coke and ore layers. To be specific, for the model used in previous sections, CO_2 is exclusively produced in ore layers and each ore layer could be treated as a source domain of CO_2 or the sink domain of CO ; however, in the model of this section, CO_2 is generated evenly in the shaft regions. As a result, the gas utilization iso-lines of these two models show different patterns.

Figure 15 shows the comparison of the top gas composition measured by industrial practice and simulated by the model with non-respective chemical reactions. Comparing Figures 11 with 15, it can be noted that both models are adequate to capture the main features of the top gas, indicating the validities and effectiveness of both models, though there are some quantitative differences between them. However, for further understanding of the internal phenomena of a BF, more details, such as the chemical reaction switching between alternative coke and ore layers, should be included. Thus, the model with respective reacting layers is more favourable for use in the future BF model investigations.

To sum up, the key features of this article include: (1) the layered burden structure with respective chemical reactions in coke and ore layers is considered in the model and (2) fluctuating iso-lines in terms of flow, temperature and concentrations can be simulated, especially the fluctuating iso-lines for gas components and three layered ferrous oxide distributions, resulting from the layered burden structure with respective chemical reactions. These effects have not been well captured in the past.

V. CONCLUSIONS

A 2D mathematical model is developed to describe the complex behaviour of multiphase flow, heat/mass transfers and chemical reactions in a BF. In this model, the respective chemical reactions in the alternate ore and coke burden layers are explicitly considered. Although

such reactions occur in real BF operations, they have not been well considered in the previous works. Typical inner furnace phenomena, such as gas and solid phase evolution and cohesive zone distribution, are simulated using this model and then compared with the simulations using a BF model without considering respective chemical reactions. The key findings are summarized as follows:

1. Temperatures of gas and solid phases show similar variation trends along the furnace height direction. However, the temperature difference between gas phase and solid phase varies in different regions, especially around the cohesive zone and near the furnace top.
2. In BF, there are three chemical reserve zones for hematite, magnetite and wustite, respectively. Inside those zones, both gas and solid components remain relatively stable.
3. The fluctuating iso-lines of gas components, gas temperature and solid temperature can be captured. They are important features of BF with layered burden and layered cohesive zone with respective chemical reactions in coke and ore layers.
4. The reduction degree of ferrous oxides shows a gradual increase from the furnace top downward with little change in chemical reserve zones. The well-developed central gas could lead to a relatively higher reduction degree in the furnace centre than in the periphery areas on the same level.

This model has provided a cost-effective way to reliably investigate the inner state of an ironmaking BF.

ACKNOWLEDGMENTS

The authors acknowledge the financial support from the Australian Research Council (LP160101100). The first author wishes to acknowledge the financial support from the China Scholarship Council.

NOMENCLATURE

SYMBOLS

A_{coke}	Effective surface area of coke for reaction (m^2)
$A_{\text{sl,d}}$	Effective contact area between solid and liquid in unit volume of bed ($\text{m}^2 \text{m}^{-3}$)
B	Basicity of slag
c_p	Specific heat ($\text{J kg}^{-1} \text{K}^{-1}$)
d_s	Diameter of solid particle (m)
D	Diffusion coefficient ($\text{m}^2 \text{s}^{-1}$)
$E_{\text{f,w}}$	Effectiveness factors of water gas reaction
$E_{\text{f,s}}$	Effectiveness factors of solution loss reaction
f_s	Conversion fraction of solid ore
F	Interaction force per unit volume (N m^{-3})
g	Gravitational acceleration (m s^{-2})

$h_{\text{l,d}}$	Dynamic hold-up of liquid phase
$h_{\text{l,t}}$	Total hold-up
h_{ij}	Heat transfer coefficient between i and j phase ($\text{W m}^{-2} \text{K}^{-1}$)
H	Enthalpy (J kg^{-1})
k_f	Gas film mass transfer coefficient (m s^{-1})
k_i	Rate constant of i th chemical reactions (m s^{-1})
K	Equilibrium constant
L_s	Node distance (m)
M_i	Molar mass of i th species in gas phase (kg mol^{-1})
N_{ore}	Number of ore particles per unit volume of bed (m^{-3})
N_{coke}	Number of coke particles per unit volume of bed (m^{-3})
Nu	Nusselt number
p	Pressure (Pa)
P	Productivity ($\text{t m}^{-3} \text{d}^{-1}$)
Pr	Prandtl number
R	Gas constant ($8.314 \text{ J K}^{-1} \text{ mol}^{-1}$)
R^*	Reaction rate ($\text{mol m}^{-3} \text{s}^{-1}$)
Re	Reynolds number
R_{ore}	Degree of reduction
S	Source term
Sc	Schmidt number
T	Temperature (K)
t_d	Elapsed time for total batch passing stockline (s)
u	Phase velocity (m s^{-1})
V_t	Total bed volume (m^3)
V_{bf}	Effective volume of BF (m^3)
V_g	Gas volume (m^3)
Vol_{cell}	Cell volume (m^3)
W_{batch}	Total batch weight of coke, ore and flux (kg)
y_i	Mole fraction of i th species in gas phase

GREEK SYMBOLS

Γ	Diffusion coefficient of general variable
\mathbf{I}	Identity tensor
ϕ	General variable
φ	Shape factor
α	Specific surface area ($\text{m}^{-2} \text{m}^{-3}$)
α_{FeO}	Activity of molten wustite
α_f, β_f	Coefficients in Ergun equation
β	Mass increase coefficient of fluid phase associated with reactions (kg mol^{-1})
χ_i	Top gas utilization efficiency
ε	Volume fraction
$\bar{\varepsilon}$	Convergence criterion
η_i	Fractional acquisition of reaction heat
λ	Thermal conductivity ($\text{W m}^{-1} \text{K}^{-1}$)
λ_{coke}	Coke ratio
λ_{flux}	Flux ratio
λ_{ore}	Ore ratio
μ	Viscosity ($\text{kg m}^{-1} \text{s}^{-1}$)
ρ	Density (kg m^{-3})
σ	Surface tension (N m^{-1})
τ	Stress tensor (Pa)

w	Mass fraction
γ	Scaling factor for convective heat transfer

SUBSCRIPTS

e	Effective
g	Gas
i	Identifier (g, s or l)
i,m	The m th species in i phase
j	Identifier (g, s or l)
k	The k th reaction
l	Liquid
l,d	Dynamic liquid
s	Solid
sm	FeO or flux in solid phase

SUPERSCRIPTS

e	Effective
g	Gas
l,d	Dynamic liquid
s	Solid
T	Transpose signal

REFERENCES

1. Y. Omori: *Blast Furnace Phenomena and Modelling*, Elsevier Applied Science, London, 1987, p. 498.
2. Y. Shimomura, K. Nishikawa, S. Arino, T. Katayama, Y. Hida, and T. Isoyama: *Tetsu-to-Hagané*, 1976, vol. 62, pp. 547–58.
3. M. Sasaki, K. Ono, A. Suzuki, Y. Okuno, K. Yoshizawa, and T. Nakamura: *Tetsu-to-Hagané*, 1976, vol. 62, pp. 559–69.
4. K. Sasaki, M. Hatano, M. Watanabe, T. Shimoda, K. Yokotani, T. Ito, and T. Yakoi: *Tetsu-to-Hagané*, 1976, vol. 62, pp. 580–91.
5. K. Kojima, T. Nist, T. Yamaguchi, H. Nakama, and S. Ida: *Tetsu-to-Hagané*, 1976, vol. 62, pp. 570–79.
6. K. Kanbara, T. Hagiwara, A. Shigemi, S. Kondo, Y. Kanayama, K. Wakabayashi, and N. Hiramoto: *Tetsu-to-Hagané*, 1976, vol. 62, pp. 535–46.
7. X.F. Dong, A.B. Yu, J. Yagi, and P. Zulli: *ISIJ Int.*, 2007, vol. 47, pp. 1553–70.
8. S. Ueda, S. Natsui, H. Nogami, J. Yagi, and T. Ariyama: *ISIJ Int.*, 2010, vol. 50, pp. 914–23.
9. S.B. Kuang, Z.Y. Li, and A.B. Yu: *Steel Res. Int.*, 2018, vol. 89, pp. 1–25.
10. P.R. Austin, H. Nogami, and J. Yagi: *ISIJ Int.*, 1997, vol. 37, pp. 748–55.
11. H. Nogami, M.S. Chu, and J. Yagi: *Comput. Chem. Eng.*, 2005, vol. 29, pp. 2438–48.
12. X.F. Dong, A.B. Yu, S.J. Chew, and P. Zulli: *Metall. Mater. Trans. B*, 2010, vol. 41B, pp. 330–49.
13. D. Fu, Y. Chen, Y.F. Zhao, J. D'Alessio, K.J. Ferron, and C.Q. Zhou: *Appl. Therm. Eng.*, 2014, vol. 66, pp. 298–308.
14. Y.S. Shen, B.Y. Guo, S. Chew, P. Austin, and A.B. Yu: *Metall. Mater. Trans. B*, 2015, vol. 46B, pp. 432–48.
15. J. Yagi, K. Taakeda, and Y. Omori: *Trans. Iron Steel Inst. Jpn.*, 1982, vol. 22, pp. 884–92.
16. P.R. Austin, H. Nogami, and J. Yagi: *ISIJ Int.*, 1997, vol. 37, pp. 458–67.
17. J. A. d. Castro, H. Nogami and J. Yagi: *ISIJ Int.*, 2000, vol. 40, pp. 637–46.
18. M.S. Chu, H. Nogami, and J. Yagi: *ISIJ Int.*, 2004, vol. 44, pp. 510–17.
19. K. Yang, S. Choi, J. Chung, and J. Yagi: *ISIJ Int.*, 2010, vol. 50, pp. 972–80.
20. S. Natsui, T. Kikuchi, and R.O. Suzuki: *Metall. Mater. Trans. B*, 2014, vol. 45B, pp. 2395–2413.
21. P. Zhou, H.L. Li, P.Y. Shi, and C.Q. Zhou: *Appl. Therm. Eng.*, 2016, vol. 95, pp. 296–302.
22. D. Fu, G.W. Tang, Y.F. Zhao, J. D'Alessio, and C.Q. Zhou: *Int. J. Heat Mass Transfer*, 2016, vol. 103, pp. 77–86.
23. D. Fu, G. Tang, Y. Zhao, J. D'Alessio, and C.Q. Zhou: *JOM*, 2018, vol. 70, pp. 951–957.
24. Z. Li, S. Kuang, A. Yu, J. Gao, Y. Qi, D. Yan, Y. Li, and X. Mao: *Metall. Mater. Trans. B*, 2018, vol. 49, pp. 1995–2010.
25. Y.S. Shen, B.Y. Guo, S. Chew, P. Austin, and A. Yu: *Metall. Mater. Trans. B*, 2016, vol. 47B, pp. 1052–62.
26. Z.Y. Li, S.B. Kuang, D.L. Yan, Y.H. Qi, and A.B. Yu: *Metall. Mater. Trans. B*, 2016, vol. 48B, pp. 602–18.
27. M. Geerdes, R. Chaigneau, and I. Kurunov: *Modern Blast Furnace Ironmaking: An Introduction*, Ios Press, Netherlands, 2015, p. 18.
28. Y.S. Shen, A.B. Yu, and P. Zulli: *Steel Res. Int.*, 2011, vol. 82, pp. 532–42.
29. D. Rangarajan, T. Shiozawa, Y.S. Shen, J.S. Curtis, and A.B. Yu: *Ind. Eng. Chem. Res.*, 2013, vol. 53, pp. 4983–90.
30. S.V. Pantakar: *Numerical Heat Transfer and Fluid Flow*, Hemisphere Publication Corporation, Washington, 1980, p. 126.
31. D.S. Gupta, J.D. Litster, V.R. Rudolph, E.T. White, and A. Domanti: *ISIJ Int.*, 1996, vol. 36, pp. 32–39.
32. G.X. Wang, S.J. Chew, A.B. Yu, and P. Zulli: *Metall. Mater. Trans. B*, 1997, vol. 28, pp. 333–43.
33. S. Ergun: *Chem. Eng. Prog.*, 1952, vol. 48, pp. 89–94.
34. W.E. Ranz and W.R. Marshall: *Chem. Eng. Prog.*, 1952, vol. 48, pp. 141–46.
35. E.R.G. Eckert and R.M. Drake: *Heat and Mass Transfer*, 2nd ed., McGrawHill, New York, 1959, p. 173.
36. P.J. Mackey and N.A. Warner: *Metal. Trans.*, 1972, vol. 3, pp. 1807–16.
37. D. Maldonado, Ph.D. thesis, UNSW, 2003.
38. I. Muchi: *TRANS ISIJ*, 1967, vol. 7, pp. 223–37.
39. S.B. Kuang, Z.Y. Li, D.L. Yan, Y.H. Qi, and A.B. Yu: *Miner. Eng.*, 2014, vol. 63, pp. 45–56.
40. S.J. Zhang, A.B. Yu, P. Zulli, B. Wright, and U. Tüzün: *ISIJ Int.*, 1998, vol. 38, pp. 1311–19.
41. B.I. Kitaev, Y.G. Yaroshenko, and V.D. Suchkov: *Heat Exchange in Shaft Furnaces*, Pergamon Press, London, 1967, p. 8.
42. Z.L. Zhang, J.L. Meng, L. Guo, and Z.C. Guo: *Metall. Mater. Trans. B*, 2016, vol. 47B, pp. 467–84.